water

MDPI

Article

Three-Dimensional Geophysical Characterization of Deeply Buried Paleokarst System in the Tahe Oilfield, Tarim Basin, China

Fei Tian [1,2,3,4], Zhongxing Wang [1,2,3,4,*], Fuqi Cheng [5], Wei Xin [6], Olalekan Fayemi [1,2,3,4], Wang Zhang [1,2,3,4] and Xiaocai Shan [1,2,3,4]

1 Key Laboratory of Shale Gas and Geoengineering, Institute of Geology and Geophysics, Chinese Academy of Sciences, Beijing 100029, China; tianfei@mail.iggcas.ac.cn (F.T.); fayemiolalekan@mail.iggcas.ac.cn (O.F.); zhangwang@mail.iggcas.ac.cn (W.Z.); shxc@mail.iggcas.ac.cn (X.S.)
2 Frontier Technology and Equipment Development Center for Deep Resources Exploration, Institute of Geology and Geophysics, Chinese Academy of Sciences, Beijing 100029, China
3 Chinese Academy of Sciences University, Beijing 100049, China
4 The Institutes of Earth Science, Chinese Academy of Sciences, Beijing 100029, China
5 School of Geosciences, China University of Petroleum, Qingdao 266580, China; chengfq9804@163.com
6 College of Information Science and Technology, Beijing University of Chemical Technology, Beijing 100029, China; xw1894@163.com
* Correspondence: zxwang@mail.iggcas.ac.cn; Tel.: +86-010-82998665

Received: 19 April 2019; Accepted: 16 May 2019; Published: 20 May 2019

Abstract: Paleokarst reservoirs are the major type of the Ordovician carbonate reservoirs in the Tahe Oilfield. Due to the strong heterogeneity in distribution, it is a real challenge to detect the spatial distribution of paleokarst reservoirs, especially those deeply buried more than 5500 m in the Tahe area. Based on the abundant core samples, this paper first described the structure of paleocaves drilled by well. Second, after time–depth conversions, the results from drilled wells were tied to three-dimensional (3D) seismic datasets, and then the threshold of host rocks and caves in wave impedance were identified. Third, the seismic-scale mapping and visualization of the paleokarst reservoirs were achieved by tracing the distribution of paleocaves. This approach was applied in the well T403 area, and the structure of the paleokarst, especially the runoff zone, was interpreted. 3D structure and spatial distribution of the paleokarst system was demonstrated by plane, vertical, and 3D models. Additionally, according to the hydrology genetic relationships, the paleocaves in the runoff zone were divided into sinkholes, main channel, and branch channel. The approach of a 3D geophysical characterization of a deeply buried paleokarst system can be applicable to Tahe and other similar paleokarst oilfields, which will guide hydrocarbon exploration in paleokarst reservoirs.

Keywords: paleokarst reservoir; three-dimensional structure; geophysical recognition; Tahe Oilfield; Tarim Basin

1. Introduction

Karst is a kind of topography that is formed by the dissolution of soluble rocks, such as limestone, dolomite, and gypsum [1–4]. It can develop a series of underground drainage systems with sinkholes and caves. The structure of these caves is very complex, often first forming some cave channels and then forming a multi-layered conduit network by changes of water table [5–9]. In the long geological history, soluble rocks are subjected to leaching by liquid, especially rainwater, for a long period. The dissolution of soluble rocks results in formation of large karst caves that formed in the vicinity of unconformity, which is called a paleokarst system [10]. Paleokarst is the general term for ancient karst features that have been fossilized

or preserved. Most commonly these features are filled with lithified sediments [11]. The underground paleokarst system can serve as an effective reservoir or oil and gas accumulation, forming some world-class oil and gas fields. Existence of examples of such fields have been reported in the Middle East [12], North America [13], and China [14–17]. Among them, the Tahe Oilfield is dominated by Ordovician carbonate karst reservoirs at a depth of more than 5500 m [18]. It is China's largest Paleozoic marine oilfield, with a hydrocarbon reserve greater than 15×10^8 m^3 [10,18]. The main storage spaces for oil and gas in the reservoirs are caves and fractures. After experiencing multiple geological processes, such as epigenetic dissolution, structural rupture, burial dissolution, collapse, and filling, the paleokarst reservoirs in the Tahe Oilfield have strong heterogeneity both vertically and horizontally [10,13,18–20]. Production proves that the productivity of the reservoirs is mainly controlled by the degree of development of caves, and the structure of the caves represents the main structure of the paleokarst reservoir [18,20].

The carbonate paleokarst reservoirs are adjacent to the paleo-weathering unconformities, with complex spatial distribution and interconnected relationships. The key problems of paleokarst reservoir research are how to accurately understand the structure of deeply buried paleokarst systems and how to use geophysical data to effectively identify their locations. Using ground penetrating radar (GPR), core samples, and typical outcrops in the Lower Ordovician Ehrenberg Group near Marble Falls in central Texas, McMechan et al. [21], and Loucks et al. [22–24] established the three-dimensional (3D) structure of a collapsed paleocave system, which became a classic model for understanding paleocaves [18,20,25–27]. Through detailed outcrop investigations and core sample observations, Tian et al. described the paleocave structure, and then used multivariate logging data to identify characteristics of subsurface paleocaves that were drilled by wells [10,26]. Using a 3D seismic amplitude dataset, Zeng et al. [27,28] and Basso et al. [29] characterized the structure of paleocave reservoirs and pointed out the associated relationship between faults and paleocaves. Sayago et al., on the other hand, used the multiple seismic attribute classification method to characterize a paleokarst system of the Loppa highlands [30]. Tian et al. used an acoustic impedance inversion dataset to identify the heterogeneity of a paleokarst system in Tarim Basin [10,31].

Considering the industrial needs of oil exploration and guided by karst hydrogeology theory, based on detailed core observation and seismic delineation, this paper characterized the 3D structure of such a deeply buried Ordovician carbonate paleokarst system in Tahe Oilfield, Tarim Basin. The results can better guide the exploration of the paleokarst reservoirs in the study area and apply it to other similar oilfields.

2. Geological Background

The Tarim Basin is located in the southern part of Xinjiang Uygur Autonomous Region, western China [32]. It is a famous multi-cycle large superimposed basin [33]. It covers an area of 56×10^4 km^2 and it is the largest onshore basin in China. Founded in 1990, the Tahe Oilfield is China's first land-based Paleozoic oilfield. The main production reservoirs of Tahe Oilfield are Ordovician strata, which formed in marine sedimentary facies in Ordovician time. As most production strata in China are terrestrial petroliferous basins, marine petroliferous basins are relatively few in China. The Tahe Oilfield is the largest marine sedimentary strata oilfield in China, with an area of about 750 km^2 [10,31]. Its geographical location is on the southern edge of the Tianshan Mountains and the northern edge of Taklimakan Desert (Figure 1), and the administrative division is located in Kuche and Luntai County, Xinjiang Uygur Autonomous Region [34–36].

Almost 30 years of exploration in the Tahe Oilfield has shown that the Arkekule Arch comprises Cambrian, Ordovician, Carboniferous, Permian, Triassic, Jurassic, Cretaceous, and Quaternary strata from bottom to top [26,37]. The main hydrocarbon producing reservoirs are in Ordovician strata, which belong to shallow sea platform-slope facies [38,39], and the caprock is Lower Carboniferous mudstone [34]. From bottom to top, there are six layers developing in the Ordovician strata, including the Lower Ordovician Penglaiba Formation (O_1p) and Yingshan Formation (O_1y), the Middle Ordovician Yijianfang Formation (O_2y), and the Upper Ordovician Group divided into the Qiaerbake Formation (O_3q), the Lianglitage Formation (O_3l), and the Sangtamu Formation (O_3s) (Figure 2) [40,41]. The target layer of this study is Ordovician Yingshan Formation (O_1y) carbonate paleokarst reservoirs.

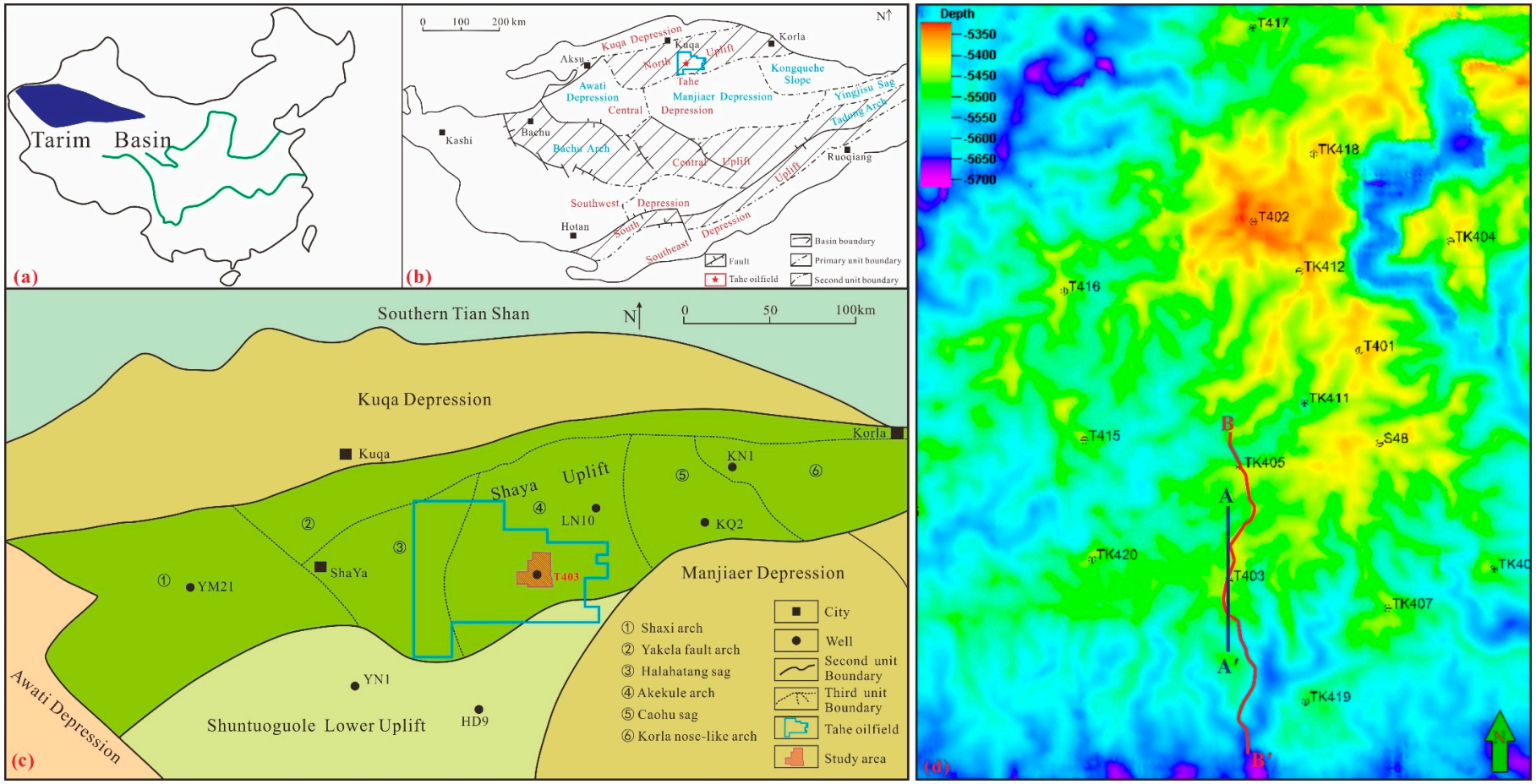

Figure 1. The structural maps of Tarim Basin and the study area, modified from Tian et al. [10,26] and Lu et al. [41]. (**a**) Tarim Basin located in western China; (**b**) The tectonic units in the Tarim Basin, mainly including four uplifts and three depressions; (**c**) The Tahe Oilfield is located in the Akekule Arch, the North Uplift of Tarim Basin; (**d**) Time domain map of Yingshan Formation buried depth.

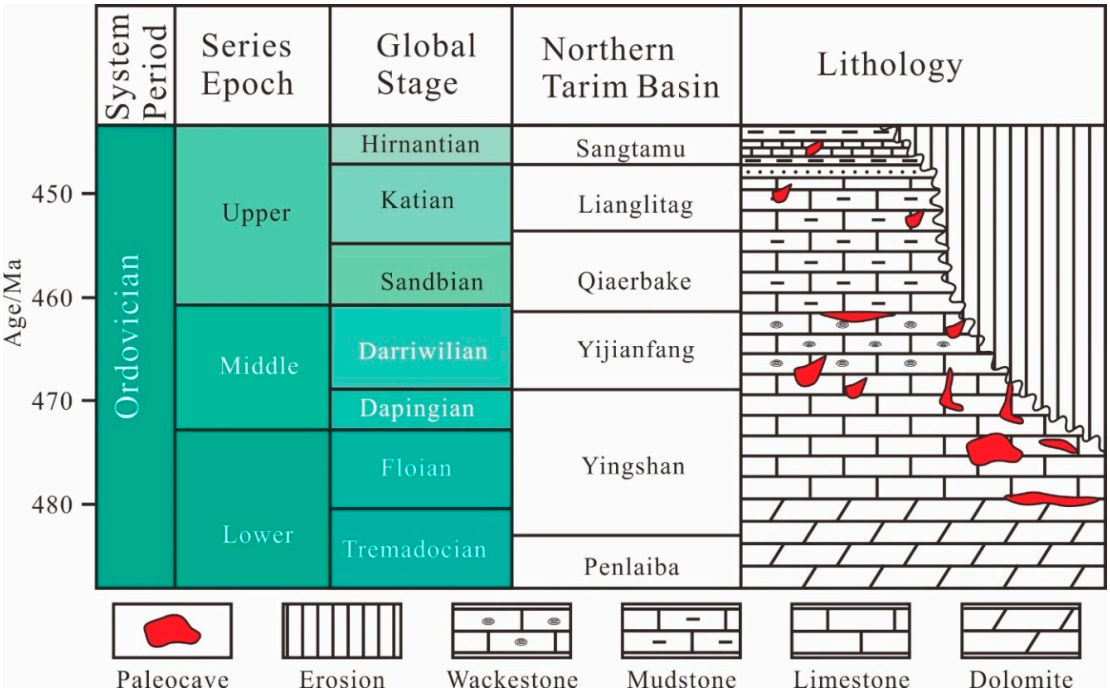

Figure 2. Chronostratigraphy and lithostratigraphy of the Tahe Oilfield, modified from Tian et al. [10,26].

The lithology of carbonate host rock is dominated by mudstone and wackestone, followed by bright-grained grainstone, and a small amount of dolomite. The multi-period fractures formed by faults and unconformities are mutually cut, combined with a variety of dissolved pores, resulting in extremely strong heterogeneity [41–45]. The paleokarst reservoirs are the main storage space and have experienced multiple stages of tectonic movements and longtime diagenetic processes [46–48]. The main karstifications were in the late Caledonian and Early Hercynian, and the karst system was buried and was not reactivated as a result of epeirogenetic movements and erosion of the overburden. In fact, these caves are not empty; they are filled by various fillings, including breccias, sedimentary fillings, and chemical fillings [10,23,26,27,41]. In present, the formation depth is generally greater than 5500 m, with ultra-high temperature (>125 °C) and high pressure (>60 MPa) [49].

3. Materials and Methods

A combination approach of core sample description, 3D seismic recognition, and modeling was used to analyze the structure of the paleokarst system. According to Loucks' typical paleocave outcrop model, the paleocaves, which are penetrated by wells, were described. Seismic datasets, whose coverage area is about 150 km^2, were used to predict the 3D spatial distribution of the interwell paleocaves. Its cell size was 15 × 15 m, and the recording length was 6 s with 2 ms sampling intervals. The seismic trace was characterized by 3000 samples with a frequency range from 3 to 85 Hz, with a dominant frequency of 26 Hz. The propagation velocity of approximately 6000 m/s was obtained for the limestone formation.

In the petroleum industry, based on the differences of lithologies' acoustic wave impedances, artificial source seismic wave exploration is one of the pillar technologies for identifying reservoirs' spatial distributions. The resolution of seismic exploration is an important parameter for identifying the geometry of the underground stratum and is generally closely related to the seismic wavelength. In other words, seismic data can certainly recognize formations with a minimum thickness of 1/4 of the seismic wavelength. Different lithologies have significantly different seismic velocities and frequencies. In clastic sandstone reservoirs, the velocity is about 2000–4000 m/s, the main frequency is 40–50 Hz, so the wavelength is about 40–100 m. The related seismic resolution in sandstone reservoirs is 10–25 m, which has been well documented in layered clastic formations. However, there are distinctly

different results in the paleokarst reservoirs of the Tahe Oilfield. There are obvious acoustic wave impedance differences between the paleokarst reservoirs and the surrounding low porosity host rocks. The paleokarst systems can be regarded as irregularly distributed, and low-speed in different sizes and shapes in uniform limestone. Regarding the detectability of paleocaves, some researchers pointed out that the fluid velocity in the caves plays an important role. Most of the reflections on seismic section are the diffraction waves of these low-speed bodies, so the paleocaves can be identified on the seismic images, which are not limited by the 1/4 wavelength [50–53]. We grasp the difference between the high-wave impedance of low porosity limestone and the low-wave impedance of the paleocaves. Using the sparse pulse inversion algorithm, the well logging data was combined with the 3D seismic amplitude data to form a high-precision impedance dataset, which could be used to obtain the boundary and distribution of the paleokarst system.

It has been realized that the geometry of modern karst systems is very irregular [54], such as Bahama Islands [55,56] and the northeast Adriatic coast [57,58], and the paleokarst system has undergone joint transformation of filling, collapse, fracture, and diagenesis, and its heterogeneity has become much more intense. The seismic profile of rule direction (positive north–south or east–west direction) cannot show the vertical structure of the irregular paleokarst reservoirs. At the same time, due to the height and undulation of the paleocaves, the detailed plane distribution of the paleokarst reservoir cannot be obtained by seismic slice at the same depth. The high-precision impedance dataset was used to delineate the 3D geometry of the paleokarst system. Firstly, the wave impedance cutoff value of the paleocaves was determined, and then the profile interpretations were performed along the central axis of the paleocaves. The third step was to interpret the profile every 50 m, and then the plane distribution map of the paleocaves was obtained. The fourth step was carrying out the vertical zonations of the paleokarst system followed by hydrogeological theory. Finally, the 3D spatial distribution of the paleokarst system was characterized by the geomodelling approach using Petrel commercial software.

4. Results

4.1. Characteristics of Paleokarst System in Tahe Oilfield

The buried depth of Ordovician paleokarst reservoirs in the Tahe Oilfield is mainly concentrated at 5300–5700 m. In fact, the oil was not generated in such depth; it was mainly (about 80%) generated in the "oil window" in 322–327 Ma, which belonged to the Middle Caledonian, with the buried depth of 2218–2453 m [59]. Due to the strong heterogeneity of the paleokarst reservoirs, the drilling success rates of different blocks in the oilfield are quite different. This distribution of oil and gas is related by many factors, such as the formation and evolution of the Akekule Arch, the characteristics of the stress field, the degree of paleokarst development, hydrocarbon accumulation conditions, and preservation conditions. Therefore, it is very important for petroleum geologists to accurately understand the characteristics of the paleokarst system in the Tahe Oilfield.

Well T403 is located in the central part of the 4th block of the Tahe Oilfield (Figure 1). It was drilled in 1999, and its target layer is the Ordovician Yingshan Formation. The well drilled through the top of the Yingshan Formation at 5387.1 m, and finished drilling at the depth of 5633.65 m. In June 1999, the first acidification and fracturing operation was carried out on carbonate strata, but there was no response. In September 1999, the second acidification and fracturing operation was carried out on carbonate strata, with maximum construction pump pressure of 74.3 Mpa. Then the oil test was conducted, resulting in average daily oil production of 187.5 m^3, and daily gas production of 18.82×10^4 m^3. Well T403 has been in a self-spraying state from September 1999 to October 2002, showing very excellent oil and gas production capacity.

As the Tahe Oilfield's key well, T403 was continuously coring between the depths of 5484.94–5490.70 m, 5504.05–5509.07 m, and 5536.52–5542.64 m. Logging interpretation shows that the well developed a cave with a height of 66.4 m at 5488.0–5554.4 m (Figure 3a), and many fractures developed at the top and bottom of the cave. The cave was almost completely filled with the collapsed

sedimentary paleokarst fillings in the longitudinal direction, including crackle breccia (Figure 3a,b), chaotic breccia (Figure 3e–g), cave-sediment fill (Figure 3c,d), and transition types (Figure 3h,i).

There are significant geophysical differences between the paleocaves and host rock sections, especially on conventional well logging responses. Compared with the host rock, the cave section has features named "three highs and two lows", including high natural gamma (GR), high acoustic time slowness (AC), high neutron porosity (CNL), low resistivity (RLLD, RLLS), and low lithology density (DEN) (Table 1, Figure 4a). As low values in acoustic velocity (v) and density (ϱ) in cave sections and high values in acoustic velocity and density in host rocks, the acoustic wave impedance ($P = \varrho \times v$) has obvious differences between them. The reflection coefficient at the interface between the cave and the host rock increases sharply. The top and bottom reflections of the cave and the secondary reflection between the top and bottom of the weak cave will be characterized by a sudden increase in amplitude on the seismic data. Seismic forward modeling and logging interpretations show that for caves with a height of >15 m, there is generally a strong bright reflection on the seismic section (Figure 4b). The acoustic impedance inversion dataset can make full use of the high-resolution information of the logging data in the vertical direction and the lateral contrastability from the amplitude seismic dataset, and has a strong recognition quality (T403 in Figure 4c).

Table 1. Well-logging responses of caves and host rock.

	CAL (in)	GR (API)	RLLD (Ω·m)	RLLS (Ω·m)	AC (μs/ft)	CNL (%)	DEN (g/cm^3)
Paleocaves	7–7.4	30–80	<700	<500	48–140	1.5–20	2.51–2.73
Host Rock	<7.1	<30	2000–20,000	1500–20,000	42–52	−1–2	2.7–2.76

Note: CAL: Caliper log, a type of well logging data which provides a continuous measurement of the size and shape of a borehole along its depth; GR: Gamma ray log, a type of well logging data which measures naturally occurring gamma radiation to characterize the rock or sediment in a borehole or drill hole. RLLD: Laterolog deep resistivity, a type of well logging data which can focuse currents to direct the path of the measured current through the mud and the invaded zone to the uninvaded formation. RLLS: Laterolog shallow resistivity, a type of well logging data which is for shallow investigation of the transition zone. AC: The acoustic log, which measures the time of transit of a sonic impulse through a given length of rock, usually 1 m. CNL: compensated neutron log, which makes thermal and epithermal neutron measurements to calculate porosity and identify lithology and the presence of gas. DEN: The density log is a continuous record of variations in the density of the lithologic column cut by the borehole.

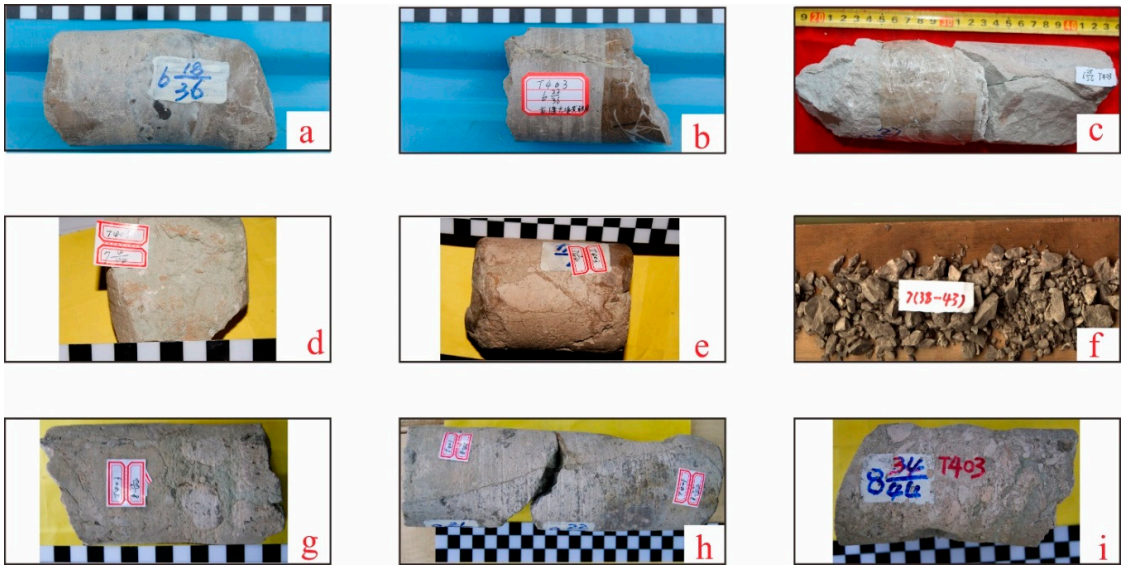

Figure 3. Core photos from well T403, illustrating the cave fillings and fractures. (**a**) The tip hole is filled with chemical filling, (**b**) fractures filled with gray–green debris filling, (**c**) light green fine debris filling, (**d**) thick debris filling, (**e**) sub-angular breccia, (**f**) angular collapsed breccia, (**g**) secondary rounded breccia with ash green fine debris filling, (**h**) coarse debris filling with breccia, (**i**) secondary round transport breccia.

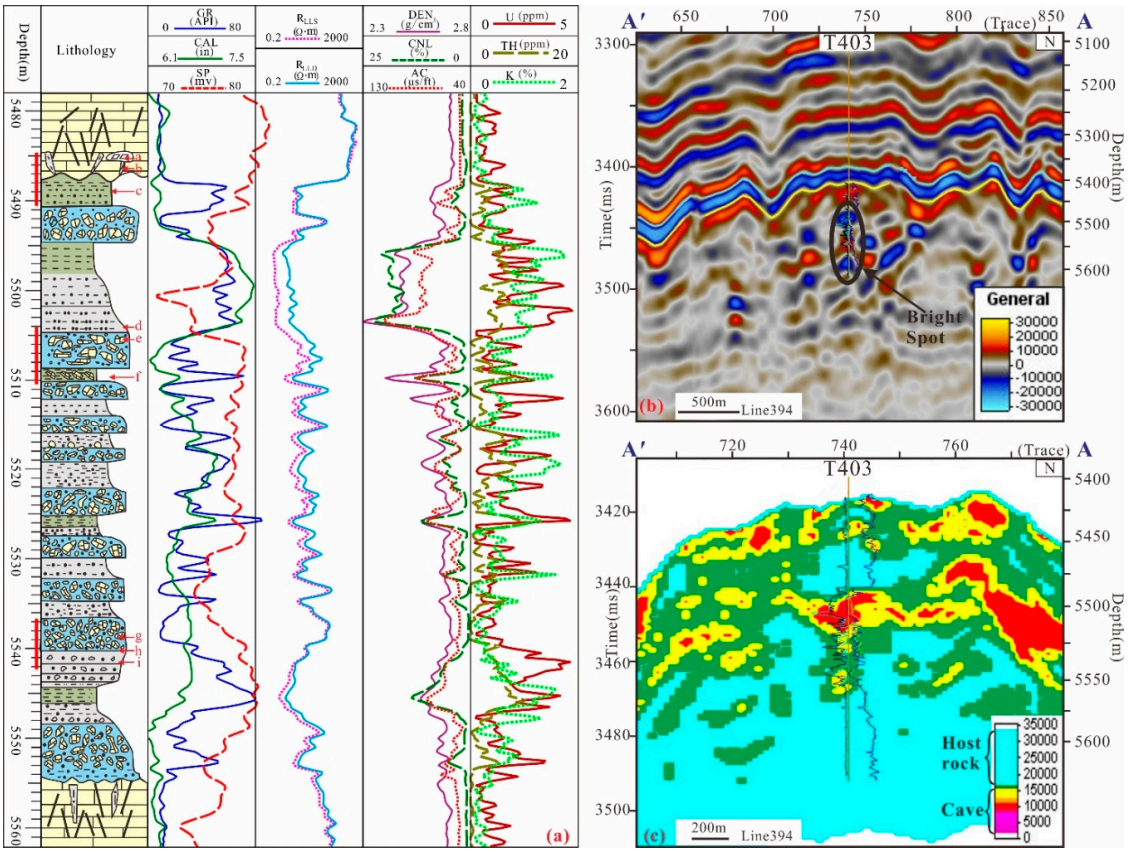

Figure 4. Comprehensive characteristics of the core, well logging, and seismic profiles of the Ordovician paleokarst reservoirs in Well T403, see profile location A-A′ in Figure 1d. (**a**) Well T403 core section comprehensive core map, showing a variety of filling inside the cave; (**b**) Well T403 amplitude seismic profile shows that the well is drilling a typical "Bright Spot"; (**c**) Well T403 wave impedance profile shows the differences between caves and host rocks.

4.2. Quantitative Seismic Identification of Paleokarst Systems

It has been established that the caves developed along fractures originally during the karstification, then the karst system was buried underground and the main storage space was in paleocaves and the fractures zones accompany the paleocaves; so this key content of the paleokarst characterization is paleocave identification [10,26]. Due to the irregular development of the paleocave, the paleocaves with heights less than 5 m produced weak responses on the seismic amplitude data, so it was very difficult to perform accurate time–depth calibration on the seismic dataset. The wellside seismic trace was first selected and its wavelet was extracted, and then the reflection coefficient was convolved to obtain the synthetic seismic record. Finally, the time–depth relationship of the well was determined. The synthetic seismogram at well T403 showed a good match with the real seismic reflection (Figure 5).

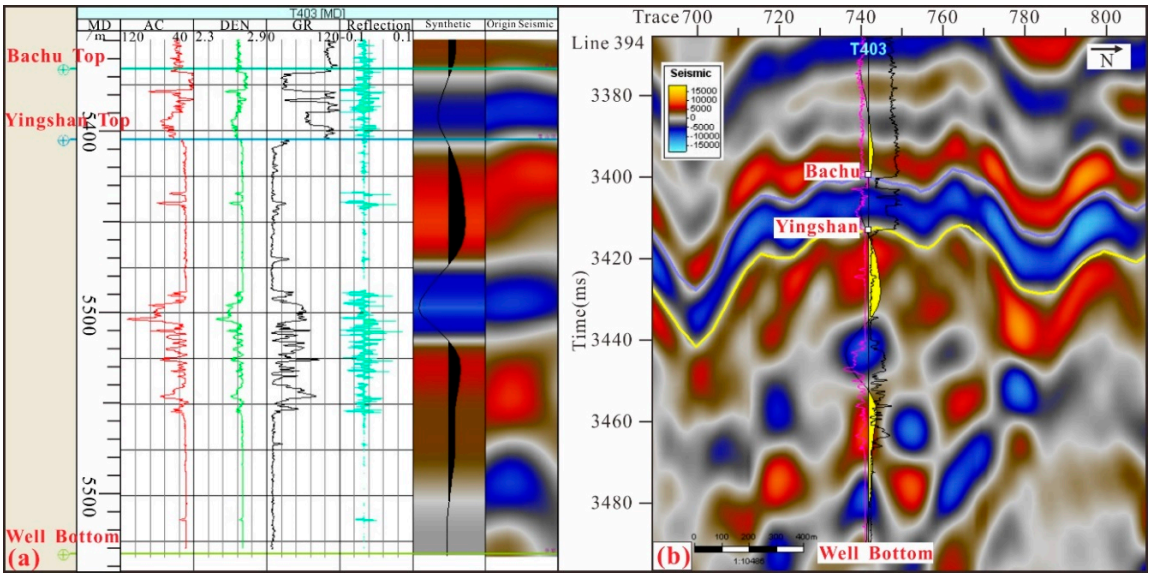

Figure 5. The synthetic seismogram at well T403, matching with the origin amplitude seismic image very well. (**a**,**b**) show that the synthetic geological record obtained by the reflection coefficient has the same peaks and troughs as the rightmost actual seismic trace.

The well logging interpretation results were calibrated on the amplitude dataset and the acoustic impedance inversion dataset. After comparison, it was found that the inversion dataset could more accurately identify the structure of the paleokarst reservoirs. In the amplitude profile, the cave (no. A4) with a height of 66.4 m in well T403 and the cave (no. C3) with a height of 21.3 m in Well TK446 had the typical "Bright Spot" reflection characteristics of the paleokarst reservoir (Table 2); The cave (no. B9) with a height of 35.9 m in well TK405 had weak reflection characteristics; other smaller caves could not be effectively identified. Moreover, the interpreters could not effectively map the interwell paleocaves' structural characteristics from the amplitude dataset (Figure 6a).

Table 2. The paleocaves drilled by wells T403, TK405, and TK446, and their recognized results by seismic datasets.

Well	no.	Cave Top (m)	Cave Bottom (m)	Cave height (m)	Cave Top to Unconformity (m)	Seismic Amplitude Dataset	Acoustic Impedance Inversion Dataset
T403	A4	5488.0	5554.4	66.4	83.0	√	√
T403	A5	5587.3	5596.6	9.3	166.5	×	√
T403	A3	5439.3	5446.3	7.0	34.3	×	√
T403	A1	5415.9	5416.2	0.3	10.9	×	≈
T403	A2	5422.2	5422.5	0.3	17.3	×	≈
TK405	B9	5459.6	5495.5	35.9	32.6	√	√
TK405	B3	5436.3	5439.6	3.3	9.3	×	√
TK405	B10	5688.3	5689.8	1.5	261.3	×	≈
TK405	B7	5443.6	5444.4	0.8	16.6	×	×
TK405	B2	5434.9	5435.5	0.6	7.9	×	×
TK405	B8	5445.3	5445.8	0.5	18.3	×	×
TK405	B5	5441.0	5441.4	0.4	14.0	×	×
TK405	B6	5441.9	5442.3	0.4	14.9	×	×
TK405	B1	5433.4	5433.8	0.4	6.4	×	×
TK405	B4	5440.1	5440.5	0.4	13.1	×	×
TK446	C3	5520.4	5541.7	21.3	25.4	√	√
TK446	C4	5587.8	5594.9	7.1	92.8	×	√
TK446	C1	5499.8	5500.8	1.0	4.8	×	×
TK446	C2	5501.8	5502.2	0.4	6.8	×	×

√: consistent, ×: inconsistent, ≈: unsure.

So as to effectively analyze the paleokarst reservoir structure, the acoustic impedance inversion dataset was used to identify the interwell paleocaves. Using the cave calibration identified by well drilling results, it was considered that the cave development section (yellow, pink, red section) was <15,300 g*s^{-1}*m^{-2}, and the non-cave development section (ice blue) was >16,500 g*s^{-1}*m^{-2}, and 15,300–16,500 g*s^{-1}*m^{-2} was the transition section (green section) (Figure 4c, Figure 6). After determining the acoustic impedance threshold, we could more effectively identify the 3D structure of the paleocaves. The caves with height 9.3 m (no. A5) and 7.0 m (no. B9) in well T403, 35.9 m (no. B9), and 3.3 m (no. B3) in well TK405, and 7.1 m (no. C4) in well TK446 were effectively identified; there were also some responses in the two adjacent 0.3 m high caves (no. A1, A2) and the 1.5 m high cave (no. B10) in the well TK405 (Table 2). The wave impedance inversion profile could not only better compare with the caves drilled by wells, but also effectively predict the interwell caves. We found the coalesced collapsed paleokarst system showed as a river shape, which could be divided into a main channel and branch channels (Figure 7). The caves between wells TK405 and T403 were characterized by a continuous underground river (Figure 6b), further confirming the reliability of the wave impedance inversion dataset.

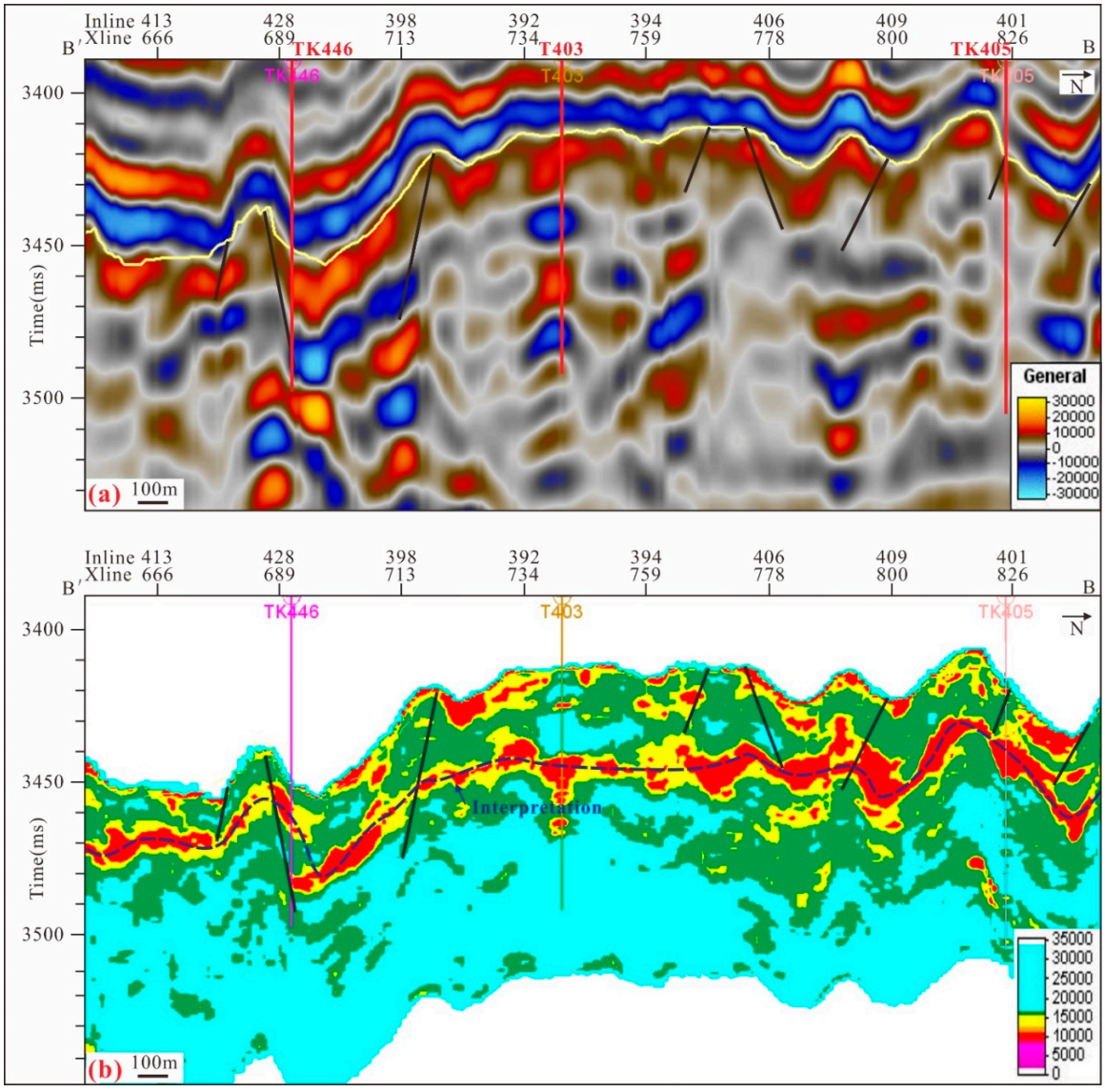

Figure 6. Different seismic profiles crossing wells TK405-T403-TK446; see profile location B-B′ in Figure 1d. (**a**) Amplitude seismic profile, (**b**) acoustic impedance inversion profile.

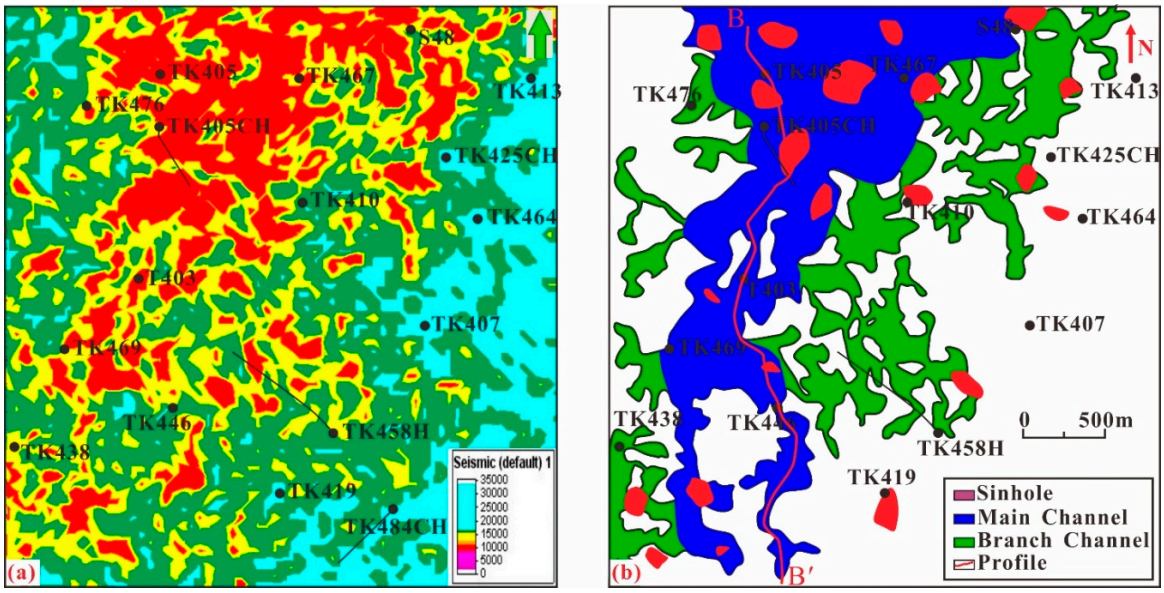

Figure 7. The interpretation results of the paleocaves in runoff zone and its geological plane. (**a**) Acoustic impedance inversion interpretation map, (**b**) corresponding geological interpretation map.

4.3. Three-Dimensional Structure of Paleokarst System

In order to obtain the 3D structural distribution characteristics of the paleokarst reservoirs, we chose the large-scale caves, and continuous caves were selected for continuous tracking (the dotted line in Figure 6b). According to the above approach, we traced the paleocaves in the well T403 area and obtained its 3D structural features. The paleocaves in this area have strong heterogeneity [60–66]: (1) In the longitudinal direction, the local area develops multiple layers of caves, and the runoff zone is the main karst development horizon; (2) In the plane view, the paleokarst main development zone show a clear genetic relationship, the branched channel shapes. Most of the rainwater in the karst area flows into the runoff zone through the sinkholes, so the sinkholes are mainly developed vertically, with a high aspect ratio (>5). In the runoff zone, the water flow is mostly horizontal, with obvious water infiltration/percolation characteristics. This zone has several main channels and branches.

The 3D structure of the paleocaves are shown in three aspects: plane views, vertical profiles, and 3D visualization model. There are 21 sinkholes, which act as the main passages to connect epikarst zone with the paleocaves in the runoff zone. In the runoff zone, there are typical branch shaped paleokarst drainage systems, including one main channel and eight branch channels in the well T403 area (Figure 7). The geometrical statistics (Table 3) indicate that, even in the karst-developed strata, the distributions of paleokarst reservoirs are strongly heterogeneous. The height of the sinkhole is generally 80–320 m, the width is 60–290 m; the length of the main channel is 3850 m, the width is 80–1930 m; the length of the branch channel is 290–1520 m, the width is 40–190 m. The paleokarst system area/total study area is 33.27%. In terms of area ratio for each genetic type, the area ratio of the sinkhole is relatively low at 11.70%, and the area ratio of the main channel, and the branch channel are 38.98% and 49.32%, respectively, in the paleokarst developing area. The volume of the main channel is the largest, accounting for 49.65% of the total paleokarst system volume; the volume ratio of the branch channel and the sinkhole are relatively low, with calculated percentage ratio values of 37.94% and 12.42%, respectively. Due to the coalesce-collapse effect during the subsequent burial process, the width and volume of the paleokarst caves became larger than the actual outcrops.

Table 3. Geometrical statistics of paleocaves in the runoff zone.

	Cave Amount	Length (m)	Width (m)	Area (m^2)	Area Ratio	Volume (m^3)	Volume/Paleokarst Volume
Sinkhole	21	80–320	60–290	897,750	11.70%	41,972,000	12.42%
Main Channel	1	3850	80–1930	2,989,575	38.98%	167,791,000	49.65%
Branch Channel	8	290–1520	40–190	3,782,475	49.32%	128,212,000	37.94%

In order to clarify the vertical development characteristics of the paleokarst conduit networks, a profile section crossing wells TK405-T403-TK446 was selected. Figure 8 shows that the paleocaves develops in a layered shape, which could be divided into epikarst zone, vadose zone, runoff zone, and phreatic zone from top to bottom [18]. The caves in the T403 well zone developed four layers, corresponding to the surface karst zone, seepage zone, runoff zone, and subsurface flow zone, and the paleokarst reservoirs in the runoff zone are most developed.

Paleokarst reservoirs can also be analyzed more intuitively through 3D engraving techniques using Petrel software. Figure 9 shows the paleocave geobody engraving results for the runoff zone. The 3D visualization structure shows that the current wells encountered the sinkhole and the main channel [67], and the next drilling considered multiple horizontal wells and high-angle wells to effectively increase the length of the wells in the paleokarst reservoir. For example, drilling a horizontal well along the top of a main channel between TK405 and T403 could effectively increase the hydrocarbon production.

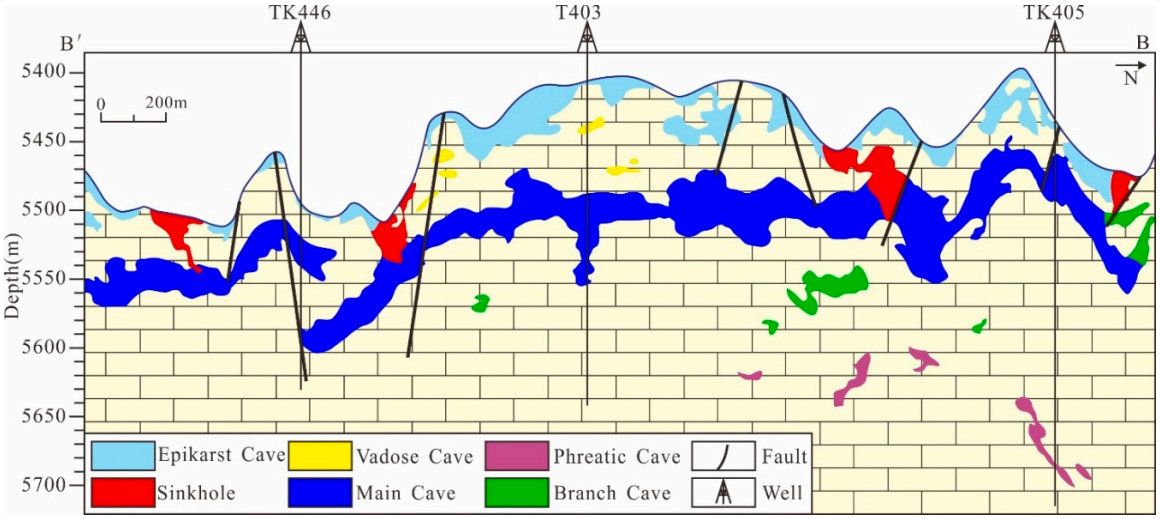

Figure 8. Geologic section crossing wells TK405-T403-TK446 regarding the structure of paleokarst reservoirs in the Tahe oilfield. Note: The amplitude seismic and acoustic impedance inversion profiles are shown in Figure 6; see the profile location B-B′ in Figures 1d and 7b.

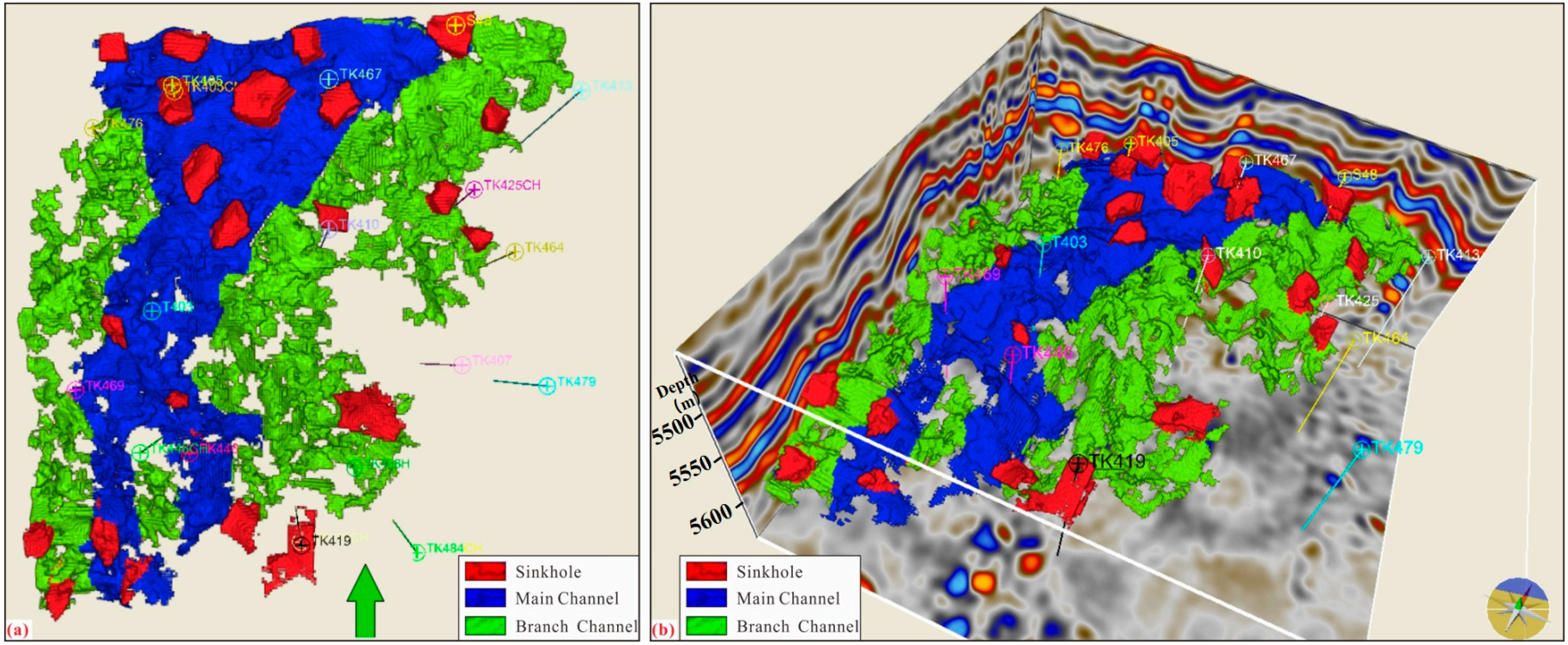

Figure 9. Three-dimensional visualization of the well T403 area genetic paleocaves in the runoff zone. (**a**) Top view of the 3D modeling result, (**b**) a depth scale view of the 3D modeling result.

5. Discussion

A karst can be a dissolved amount of pore space transformed from limestone, thus becoming an effective reservoir of groundwater or hydrocarbons [68,69]. A large number of oil and gas reservoirs in carbonate karsted formations have been discovered. However, these reservoirs are highly heterogeneous, and seismic amplitude datasets can only be used to identify some larger paleokarst caves with heights greater than 15 m. Using a high-precision acoustic impedance seismic dataset, combined with core observation and logging interpretation results, the 3D characterization of the paleokarst system in the Tahe Oilfield was carried out. The 3D structure and spatial distribution of the paleokarst system was demonstrated by plane, vertical, and 3D model.

The development of paleocaves is controlled by karstification and is subject to the transformation of subsequent geological processes, such as faulting and diagenesis [41,70–73]. The classification of paleocaves in the runoff zone (consisting of an oscillation zone and a shallow phreatic zone, which are typically indistinguishable in paleokarst system) was carried out by following the engineering classification scheme of the paleokarst system in the Tahe Oilfield [10,18]. More importantly, based on the difference in wave impedance between the host rock and the paleocaves, the acoustic impedance inversion dataset was used to identify paleocaves with height about 3 m (Table 2), so that the 3D structure of paleokarst could be displayed. The carving of paleocaves provides a practical case for a detailed understanding of such deeply buried paleokarst systems.

As hydrocarbon are stored in the pore systems in reservoirs, it is important to predict the porous sweet spots, especially in the deeply buried paleokarst system. The core observation shows that the paleocave filling is very complicated and has strong heterogeneity. The filling characteristics of these deeply buried paleocaves, including breccias, sedimentary fillings, and chemical fillings, are similar to those of the paleocaves found in outcrops [26]. The core shows that the fillings in the paleocaves are thin and interbedded, reflecting the multi-period and turbulent humid environment in which the development of the filling occurred, which is consistent with the process of frequent renovation, abandonment, and filling of cave systems in modern karst [74]. We believe that a detailed evaluation of the petrophysical characteristics of these cave fillings and a summary of their filling laws are of great significance for oil and gas exploration [75,76].

Integrating seismic exploration with electromagnetic exploration results can provide solid technical support for efficient exploration of paleokarst reservoirs in further studies. Artificial seismic data uses seismic elastic waves for deep stratigraphic exploration, showing the geologic structure of deep geology. The actual exploration of the oilfield shows that the distribution of oil and gas in the paleokarst system is very complicated. How to improve the success rate of deep reservoir exploration is a permanent problem in the petroleum industry. Di et al. measured the electrical information of the strata by means of electromagnetic exploration, detected the complex terrain, complex media, fine structures, and water-bearing features within engineering structures [77–79]. It has been successfully applied in the areas of Alashan in the Inner Mongolia Autonomous Region and Fengtai in Shaanxi Province, and found abundant mineral resources [80–82]. We believe that the close integration of seismic exploration and electromagnetic exploration can not only identify the positions of the deep paleokarst system, but also effectively predict the fluid properties of the paleokarst reservoirs, which can provide technical support for the efficient exploration of paleokarst reservoirs.

6. Conclusions

The paleokarst system of the Tahe Oilfield contains abundant oil and natural gas resources, although the current hydrocarbon production reservoirs are deeply buried at 5300–5700 m. These reservoirs are highly heterogeneous, and seismic amplitude dataset can only be used to identify some larger paleocaves with heights greater than 15 m. An acoustic impedance inversion seismic dataset was used to describe the deep paleokarst reservoirs in the Tahe Oilfield. We found that the paleocave development section was less than 15,300 $g^{*}s^{-1}{*}m^{-2}$, and the results had a good correspondence with paleocaves drilled by wells, with a relative vertical resolution of 3 m.

The geodetic development features of the runoff zone in the well T403 area were described by plane analysis, profile interpretation, and 3D modeling. According to karst hydrology and geological classification of paleokarst reservoirs, 21 sinkholes, one main channel, and eight branch channels were recognized in the study area. Quantitative statistics results showed that the volume of the main channel is the largest among the three types, which is the most favorable reservoir development position. We suggest that the next step of exploration can include drilling horizontal wells and high-angle wells in the main development area of the main channel and the branch channels to improve hydrocarbon production.

The geophysical data was used to quantitatively characterize the strong heterogeneity of the paleokarst conduit network. The obtained results provide reliable material for the correct establishment of the geological model of the paleokarst reservoirs, which can guide hydrocarbon exploration in Tahe or other similar oilfields. It is recommended to quantitatively evaluate the petrophysical characteristics of the paleocave fillings and summarize the distributions of breccias, sedimentary fillings, and chemical fillings. We suggest that integrating seismic exploration with electromagnetic exploration results can provide solid technical support for efficient exploration of paleokarst reservoirs.

Author Contributions: Conceptualization, F.T. and Z.W.; methodology, F.T. and F.C.; software, F.T. and Z.W.; validation, Z.W., F.C., and W.X.; formal analysis, O.F.; investigation, W.Z. and X.S.; resources, F.T. and F.C.; data curation, F.T. and F.C.; writing—original draft preparation, F.T. and Z.W.; writing—review and editing, O.F. and X.S.; visualization, W.Z.; supervision, F.T. and Z.W.; project administration, F.T., Z.W., and F.C.; funding acquisition, Z.W.

Funding: This study was supported by Youth Innovation Promotion Association CAS (Grant No. 81709990), CAS Key Technology Talent Program (Grant No. 81761469), the Chinese National Natural Science Foundation (Grant No. 41502149, No. U1663204, and No. 41504142), the Strategic Priority Research Program of the Chinese Academy of Sciences (Grant No. XDA14050101), the Chinese National Major Fundamental Research Developing Project (Grant No. 2017ZX05008-004 and 2016ZX05014-002), and the Fundamental Research Funds for the Central Universities (ZY1927).

Acknowledgments: We thank Schlumberger for granting Institute of Geology and Geophysics, Chinese Academy of Sciences, an academic license for Petrel software. We thank two anonymous reviewers and academic editor. Their thorough and critical reviews and suggestions have significantly improved the manuscript.

Conflicts of Interest: The authors declare no conflict of interest.

References

1. Ford, D. Jovan Cvijic and the founding of karst geomorphology. *Environ. Geol.* **2007**, *51*, 675–684. [CrossRef]
2. Ford, D.C. Karst geomorphology, caves and cave deposits: A review of North American contributions during the past half century. *Geol. Soc. Am. Spec. Pap.* **2006**, *404*, 1–13. [CrossRef]
3. Qi, J.H.; Xu, M.; Cen, X.Y.; Wang, L.; Zhang, Q. Characterization of Karst Conduit Network Using Long-Distance Tracer Test in Lijiang, Southwestern China. *Water* **2018**, *10*, 949. [CrossRef]
4. Zheng, X.Q.; Wang, K.; Zhang, F.; Chen, J.F.; Li, A.M.; Chen, Y.P. Analysis of the Erosion Law of Karst Groundwater Using Hydrogeochemical Theory in Liulin Spring Area, North China. *Water* **2018**, *10*, 674. [CrossRef]
5. Zhang, Z.X.; Wang, W.P.; Qu, S.S.; Huang, Q.; Liu, S.; Xu, Q.Y.; Ni, L.D. A New Perspective to Explore the Hydraulic Connectivity of Karst Aquifer System in Jinan Spring Catchment, China. *Water* **2018**, *10*, 1368. [CrossRef]
6. Delle Rose, M.; Martano, P. Infiltration and Short-Time Recharge in Deep Karst Aquifer of the Salento Peninsula (Southern Italy): An Observational Study. *Water* **2018**, *10*, 260. [CrossRef]
7. Dvory, N.Z.; Ronen, A.; Livshitz, Y.; Adar, E.; Kuznetsov, M.; Yakirevich, A. Quantification of Groundwater Recharge from an Ephemeral Stream into a Mountainous Karst Aquifer. *Water* **2018**, *10*, 79. [CrossRef]
8. Liu, L.Y.; Guan, D.J.; Yang, Q.W. Evaluation of Water Resource Security Based on an MIV-BP Model in a Karst Area. *Water* **2018**, *10*, 786. [CrossRef]
9. Huang, D.; Liu, Z.B.; Wang, W.K. Evaluating the Impaction of Coal Mining on Ordovician Karst Water through Statistical Methods. *Water* **2018**, *10*, 1409. [CrossRef]

10. Tian, F.; Di, Q.; Jin, Q.; Cheng, F.; Zhang, W.; Lin, L.; Wang, Y.; Yang, D.; Niu, C.; Li, Y. Multiscale geological-geophysical characterization of the epigenic origin and deeply buried paleokarst system in Tahe Oilfield, Tarim Basin. *Mar. Petrol. Geol.* **2019**, *102*, 16–32. [CrossRef]
11. Simms, M.J. Karst and Paleokarst. In *Reference Module in Earth Systems and Environmental Sciences*; Elsevier: Amsterdam, The Netherlands, 2014. [CrossRef]
12. Burberry, C.M.; Jackson, C.A.L.; Chandler, S.R. Seismic reflection imaging of karst in the Persian Gulf: Implications for the characterization of carbonate reservoirs. *AAPG Bull.* **2016**, *100*, 1561–1584. [CrossRef]
13. Russel-Houston, J.; Gray, K. Paleokarst in the Grosmont Formation and reservoir implications, Saleski, Alberta, Canada. *Interpretation* **2014**, *2*, Sf29–Sf50. [CrossRef]
14. Chen, Z.H.; Wang, T.G.; Li, M.J.; Yang, F.L.; Chen, B. Biomarker geochemistry of crude oils and Lower Paleozoic source rocks in the Tarim Basin, western China: An oil-source rock correlation study. *Mar. Petrol. Geol.* **2018**, *96*, 94–112. [CrossRef]
15. Gao, D.; Lin, C.S.; Hu, M.Y.; Yang, H.J.; Huang, L.L. Paleokarst of the Lianglitage Formation related to tectonic unconformity at the top of the Ordovician in the eastern Tazhong Uplift, Tarim Basin, NW China. *Geol. J.* **2018**, *53*, 458–474. [CrossRef]
16. Jiang, L.; Cai, C.F.; Worden, R.H.; Crowley, S.F.; Jia, L.Q.; Zhang, K.; Duncan, I.J. Multiphase dolomitization of deeply buried Cambrian petroleum reservoirs, Tarim Basin, north-west China. *Sedimentology* **2016**, *63*, 2130–2157. [CrossRef]
17. Jiang, L.; Worden, R.H.; Cai, C.F.; Shen, A.J.; He, X.Y.; Pan, L.Y. Contrasting diagenetic evolution patterns of platform margin limestones and dolostones in the Lower Triassic Feixianguan Formation, Sichuan Basin, China. *Mar. Petrol. Geol.* **2018**, *92*, 332–351. [CrossRef]
18. Tian, F.; Jin, Q.; Lu, X.B.; Lei, Y.H.; Zhang, L.K.; Zheng, S.Q.; Zhang, H.F.; Rong, Y.S.; Liu, N.G. Multi-layered ordovician paleokarst reservoir detection and spatial delineation: A case study in the Tahe Oilfield, Tarim Basin, Western China. *Mar. Petrol. Geol.* **2016**, *69*, 53–73. [CrossRef]
19. Zhu, G.Y.; Zhang, Z.Y.; Zhou, X.X.; Yan, L.; Sun, C.H.; Zhao, B. Preservation of Ultradeep Liquid Oil and Its Exploration Limit. *Energy Fuel* **2018**, *32*, 11165–11176. [CrossRef]
20. Li, Y.Q.; Hou, J.G.; Sun, J.F.; Kang, Z.J.; Liu, Y.M.; Song, S.H.; Han, D. Paleokarst reservoir features and their influence on production in the Tahe Oilfield, Tarim basin, China. *Carbonate Evaporite* **2018**, *33*, 705–716. [CrossRef]
21. McMechan, G.A.; Loucks, R.G.; Zeng, X.X.; Mescher, P. Ground penetrating radar imaging of a collapsed paleocave system in the Ellenburger dolomite, central Texas. *J. Appl. Geophys.* **1998**, *39*, 1–10. [CrossRef]
22. Loucks, R.G. Paleocave carbonate reservoirs: Origins, burial-depth modifications, spatial complexity, and reservoir implications. *AAPG Bull.* **1999**, *83*, 1795–1834.
23. Loucks, R.G.; Mescher, P.K.; McMechan, G.A. Three-dimensional architecture of a coalesced, collapsed-paleocave system in the Lower Ordovician Ellenburger Group, central Texas. *AAPG Bull.* **2004**, *88*, 545–564. [CrossRef]
24. Loucks, R.G. A review of coalesced, collapsed-paleocave systems and associated suprastratal deformation. *Acta Carsol.* **2007**, *36*, 121–132. [CrossRef]
25. McDonnell, A.; Loucks, R.G.; Dooley, T. Quantifying the origin and geometry of circular sag structures in northern Fort Worth Basin, Texas: Paleocave collapse, pull-apart fault systems, or hydrothermal alteration? *AAPG Bull.* **2007**, *91*, 1295–1318. [CrossRef]
26. Tian, F.; Lu, X.B.; Zheng, S.Q.; Zhang, H.F.; Rong, Y.S.; Yang, D.B.; Liu, N.G. Structure and Filling Characteristics of Paleokarst Reservoirs in the Northern Tarim Basin, Revealed by Outcrop, Core and Borehole Images. *Open Geosci.* **2017**, *9*, 266–280. [CrossRef]
27. Zeng, H.L.; Loucks, R.; Janson, X.; Wang, G.Z.; Xia, Y.P.; Yuan, B.H.; Xu, L.G. Three-dimensional seismic geomorphology and analysis of the Ordovician paleokarst drainage system in the central Tabei Uplift, northern Tarim Basin, western China. *AAPG Bull.* **2011**, *95*, 2061–2083. [CrossRef]
28. Zeng, H.L.; Wang, G.Z.; Janson, X.; Loucks, R.; Xia, Y.P.; Xu, L.G.; Yuan, B.H. Characterizing seismic bright spots in deeply buried, Ordovician Paleokarst strata, Central Tabei uplift, Tarim Basin, Western China. *Geophysics* **2011**, *76*, B127–B137. [CrossRef]
29. Basso, M.; Kuroda, M.C.; Afonso, L.C.S.; Vidal, A.C. Three-Dimensional Seismic Geomorphology of Paleokarst in the Cretaceous Macae Group Carbonates, Campos Basin, Brazil. *J. Petrol. Geol.* **2018**, *41*, 513–526. [CrossRef]

30. Sayago, J.; Di Lucia, M.; Mutti, M.; Cotti, A.; Sitta, A.; Broberg, K.; Przybylo, A.; Buonaguro, R.; Zimina, O. Characterization of a deeply buried paleokarst terrain in the Loppa High using core data and multiattribute seismic facies classification. *AAPG Bull.* **2012**, *96*, 1843–1866. [CrossRef]
31. Tian, F.; Luo, X.R.; Zhang, W. Integrated geological-geophysical characterizations of deeply buried fractured-vuggy carbonate reservoirs in Ordovician strata, Tarim Basin. *Mar. Petrol. Geol.* **2019**, *99*, 292–309. [CrossRef]
32. Zhu, G.Y.; Zhang, Y.; Zhou, X.X.; Zhang, Z.Y.; Du, D.D.; Shi, S.B.; Li, T.T.; Chen, W.Y.; Han, J.F. TSR, deep oil cracking and exploration potential in the Hetianhe gas field, Tarim Basin, China. *Fuel* **2019**, *236*, 1078–1092. [CrossRef]
33. Zhang, H.; Cai, Z.X.; Hao, F.; Qi, L.X.; Yun, L.; Jiang, L. Hydrogeomorphologic architecture of epikarst reservoirs in the Middle-Lower Ordovician, Tazhong Uplift, Tarim Basin, China. *Mar. Petrol. Geol.* **2018**, *98*, 146–161. [CrossRef]
34. Lu, X.X.; Wang, Y.F.; Yu, H.F.; Bai, Z.K. Major factors affecting the closure of marine carbonate caprock and their quantitative evaluation: A case study of Ordovician rocks on the northern slope of the Tazhong uplift in the Tarim Basin, western China. *Mar. Petrol. Geol.* **2017**, *83*, 231–245. [CrossRef]
35. Wang, Y.Y.; Chen, J.F.; Pang, X.Q.; Zhang, B.S.; Chen, Z.Y.; Zhang, G.Q.; Luo, G.P.; He, L.W. Origin of deep sour natural gas in the Ordovician carbonate reservoir of the Tazhong Uplift, Tarim Basin, northwest China: Insights from gas geochemistry and formation water. *Mar. Petrol. Geol.* **2018**, *91*, 532–549. [CrossRef]
36. Zhan, Z.W.; Zou, Y.R.; Pan, C.C.; Sun, J.N.; Lin, X.H.; Peng, P.A. Origin, charging, and mixing of crude oils in the Tahe oilfield, Tarim Basin, China. *Org. Geochem.* **2017**, *108*, 18–29. [CrossRef]
37. Li, Y.Q.; Hou, J.G.; Ma, X.Q. Data integration in characterizing a fracture-cavity reservoir, Tahe oilfield, Tarim basin, China. *Arab. J. Geosci.* **2016**, *9*, 532. [CrossRef]
38. Zhu, G.Y.; Milkov, A.V.; Chen, F.R.; Weng, N.; Zhang, Z.Y.; Yang, H.J.; Liu, K.Y.; Zhu, Y.F. Non-cracked oil in ultra-deep high-temperature reservoirs in the Tarim basin, China. *Mar. Petrol. Geol.* **2018**, *89*, 252–262. [CrossRef]
39. Zhu, G.Y.; Wang, M.; Zhang, T.W. Identification of polycyclic sulfides hexahydrodibenzothiophenes and their implications for heavy oil accumulation in ultra-deep strata in Tarim Basin. *Mar. Petrol. Geol.* **2016**, *78*, 439–447. [CrossRef]
40. Zhang, Q.Y.; Qin, F.R.; Liang, B.; Cao, J.W.; Dan, Y.; Li, J.R.; Chen, L.X. Characteristics of Ordovician paleokarst inclusions and their implications for paleoenvironmental and geological history in Halahatang area of northern Tarim Basin. *Carbonate Evaporite* **2018**, *33*, 43–54. [CrossRef]
41. Lu, X.B.; Wang, Y.; Tian, F.; Li, X.H.; Yang, D.B.; Li, T.; Lv, Y.P.; He, X.M. New insights into the carbonate karstic fault system and reservoir formation in the Southern Tahe area of the Tarim Basin. *Mar. Petrol. Geol.* **2017**, *86*, 587–605. [CrossRef]
42. Ma, D.; Cai, X.; Li, Q.; Duan, H.Y. In-Situ and Numerical Investigation of Groundwater Inrush Hazard from Grouted Karst Collapse Pillar in Longwall Mining. *Water* **2018**, *10*, 1187. [CrossRef]
43. Lyu, X.X.; Tao, Z.; Gao, Q.Z.; Peng, H.X.; Zhou, M. Chemical Weathering and Riverine Carbonate System Driven by Human Activities in a Subtropical Karst Basin, South China. *Water* **2018**, *10*, 1524. [CrossRef]
44. Pang, X.Q.; Jia, C.Z.; Pang, H.; Yang, H.J. Destruction of hydrocarbon reservoirs due to tectonic modifications: Conceptual models and quantitative evaluation on the Tarim Basin, China. *Mar. Petrol. Geol.* **2018**, *91*, 401–421. [CrossRef]
45. Yuan, J.F.; Xu, F.; Deng, G.S.; Tang, Y.Q.; Li, P.Y. Hydrogeochemistry of Shallow Groundwater in a Karst Aquifer System of Bijie City, Guizhou Province. *Water* **2017**, *9*, 625. [CrossRef]
46. Zhu, G.Y.; Zhang, Y.; Wang, M.; Zhang, Z.Y. Discovery of High-Abundance Diamondoids and Thiadiamondoids and Severe TSR Alteration of Well ZS1C Condensate, Tarim Basin, China. *Energy Fuel* **2018**, *32*, 7383–7392. [CrossRef]
47. Zhang, Y.F.; Tan, F.; Qu, H.Z.; Zhong, Z.Q.; Liu, Y.; Luo, X.S.; Wang, Z.Y.; Qu, F. Karst monadnock fine characterization and reservoir control analysis: A case from Ordovician weathering paleokarst reservoirs in Lungu area, Tarim Basin, NW China. *Petrol. Explor. Dev.* **2017**, *44*, 758–769. [CrossRef]
48. Zhang, Y.Y.; Sun, Z.D.; Han, J.F.; Wang, H.Y.; Fan, C.Y. Fluid mapping in deeply buried Ordovician paleokarst reservoirs in the Tarim Basin, western China. *Geofluids* **2016**, *16*, 421–433. [CrossRef]

49. Zhu, G.Y.; Zhang, Y.; Zhang, Z.Y.; Li, T.T.; He, N.N.; Grice, K.; Neng, Y.; Greenwood, P. High abundance of alkylated diamondoids, thiadiamondoids and thioaromatics in recently discovered sulfur-rich LS2 condensate in the Tarim Basin. *Org. Geochem.* **2018**, *123*, 136–143. [CrossRef]
50. Liu, W.; Zhang, L.K.; Liu, P.Y.; Qin, X.Q.; Shan, X.J.; Yao, X. FDOM Conversion in Karst Watersheds Expressed by Three-Dimensional Fluorescence Spectroscopy. *Water* **2018**, *10*, 1427. [CrossRef]
51. Shan, X.; Tian, F.; Cheng, F.; Yang, C.; Xin, W. Spectral Decomposition and a Waveform Cluster to Characterize Strongly Heterogeneous Paleokarst Reservoirs in the Tarim Basin, China. *Water* **2019**, *11*, 256. [CrossRef]
52. Di, Q.Y.; Zhang, M.G.; Wang, M.Y. Time-domain inversion of GPR data containing attenuation resulting from conductive losses. *Geophysics* **2006**, *71*, K103–K109. [CrossRef]
53. Tian, F.; Wang, W.; Liu, N.; Jiang, J.; Niu, C.; Zhang, Y.; Li, Y. Rock-Type Definition and Pore Characterization of Tight Carbonate Rocks Based on Thin Sections and MICP and NMR Experiments. *Appl. Magn. Reson.* **2018**, *49*, 631–652. [CrossRef]
54. Jebreen, H.; Banning, A.; Wohnlich, S.; Niedermayr, A.; Ghanem, M.; Wisotzky, F. The Influence of Karst Aquifer Mineralogy and Geochemistry on Groundwater Characteristics: West Bank, Palestine. *Water* **2018**, *10*, 1829. [CrossRef]
55. Mylroie, J.; Vacher, H. A conceptual view of carbonate island karst. *Karst Model. Karst Waters Inst. Spec. Publ.* **1999**, *5*, 48–57.
56. Mylroie, J.E.; Mylroie, J.R. Caves and karst of the Bahama Islands. In *Coastal Karst Landforms*; Springer: London, UK, 2013; pp. 147–176.
57. Surić, M.; Juračić, M.; Horvatinčić, N.; Bronić, I.K. Late Pleistocene–Holocene sea-level rise and the pattern of coastal karst inundation: Records from submerged speleothems along the Eastern Adriatic Coast (Croatia). *Mar. Geol.* **2005**, *214*, 163–175. [CrossRef]
58. Furlani, S.; Cucchi, F.; Forti, F.; Rossi, A. Comparison between coastal and inland Karst limestone lowering rates in the northeastern Adriatic Region (Italy and Croatia). *Geomorphology* **2009**, *104*, 73–81. [CrossRef]
59. Dan, R.; Qin, J.; Jin, X.; Shi, W.; Zhang, Z.; Xi, B.; Tao, G.; Hong, J.J. Accumulation periods of Ordovician reservoirs in Tahe Oil Field. *Petrol. Geol. Exp.* **2014**, *36*, 83–88.
60. Di, Q.Y.; Zhang, M.G.; Wang, M.Y. Time-domain finite-element wave form inversion of acoustic wave equation. *J. Comput. Acoust.* **2004**, *12*, 387–396. [CrossRef]
61. Shah, R.A.; Jeelani, G.; Goldscheider, N. Karst Geomorphology, Cave Development and Hydrogeology in the Kashmir Valley, Western Himalaya, India. *Acta Carsol.* **2018**, *47*, 5–21.
62. Vardanjani, H.K.; Chitsazan, M.; Ford, D.; Karimi, H.; Charchi, A. Initial assessment of recharge areas for large karst springs: A case study from the central Zagros Mountains, Iran. *Hydrogeol. J.* **2018**, *26*, 57–70. [CrossRef]
63. Zhang, Z.Y.; Zhu, G.Y.; Zhang, Y.J.; Han, J.F.; Li, T.T.; Wang, E.Z.; Greenwood, P. The origin and accumulation of multi-phase reservoirs in the east Tabei uplift, Tarim Basin, China. *Mar. Petrol. Geol.* **2018**, *98*, 533–553. [CrossRef]
64. Malenica, L.; Gotovac, H.; Kamber, G.; Simunovic, S.; Allu, S.; Divic, V. Groundwater Flow Modeling in Karst Aquifers: Coupling 3D Matrix and 1D Conduit Flow via Control Volume Isogeometric AnalysisExperimental Verification with a 3D Physical Model. *Water* **2018**, *10*, 1787. [CrossRef]
65. Mansour, M.; Peach, D.; Robins, N.; Hughes, A. Using a Distributed Recharge Model to Quantify Recharge Processes in a Semi-Arid Karst Catchment: An Example from Wadi Natuf, West Bank. *Water* **2019**, *11*, 276. [CrossRef]
66. Xue, Y.; Teng, T.; Zhu, L.; He, M.M.; Ren, J.; Dong, X.; Liu, F. Evaluation of the Non-Darcy Effect of Water Inrush from Karst Collapse Columns by Means of a Nonlinear Flow Model. *Water* **2018**, *10*, 1234. [CrossRef]
67. Zheng, X.Q.; Zang, H.F.; Zhang, Y.B.; Chen, J.F.; Zhang, F.; Shen, Y. A Study of Hydrogeochemical Processes on Karst Groundwater Using a Mass Balance Model in the Liulin Spring Area, North China. *Water* **2018**, *10*, 903. [CrossRef]
68. Xing, L.T.; Huang, L.X.; Chi, G.Y.; Yang, L.Z.; Li, C.S.; Hou, X.Y. A Dynamic Study of a Karst Spring Based on Wavelet Analysis and the Mann-Kendall Trend Test. *Water* **2018**, *10*, 698. [CrossRef]
69. Zheng, Q.W.; Su, W.C.; Zhang, F.T.; Zhou, Z.Q. Evaluation of Water Resources Security in the Karst Region from the "Man-Land-Water" Perspective: A Case Study of Guizhou Province. *Water* **2019**, *11*, 224. [CrossRef]
70. May, M.T.; Brackman, T.B. Geophysical characterization of karst landscapes in Kentucky as modern analogs for paleokarst reservoirs. *Interpretation* **2014**, *2*, Sf51–Sf63. [CrossRef]

71. Yang, W.M.; Fang, Z.D.; Yang, X.; Shi, S.S.; Wang, J.; Wang, H.; Bu, L.; Li, L.P.; Zhou, Z.Q.; Li, X.Q. Experimental Study of Influence of Karst Aquifer on the Law of Water Inrush in Tunnels. *Water* **2018**, *10*, 1211. [CrossRef]
72. Yu, J.B.; Li, Z.; Yang, L. Fault system impact on paleokarst distribution in the Ordovician Yingshan Formation in the central Tarim basin, northwest China. *Mar. Petrol. Geol.* **2016**, *71*, 105–118. [CrossRef]
73. Yu, J.B.; Li, Z.; Yang, L.; Han, Y.X. Model identification and control of development of deeply buried paleokarst reservoir in the central Tarim Basin, northwest China. *J. Geophys. Eng.* **2018**, *15*, 576–592. [CrossRef]
74. Jia, Z.X.; Zang, H.F.; Zheng, X.Q.; Xu, Y.X. Climate Change and Its Influence on the Karst Groundwater Recharge in the Jinci Spring Region, Northern China. *Water* **2017**, *9*, 267. [CrossRef]
75. Fu, Q.L. Characterization and discrimination of paleokarst breccias and pseudobreccias in carbonate rocks: Insight from Ordovician strata in the northern Tarim Basin, China. *Sediment. Geol.* **2019**, *382*, 61–74. [CrossRef]
76. Husic, A.; Fox, J.; Agouridis, C.; Currens, J.; Ford, W.; Taylor, C. Sediment carbon fate in phreatic karst (Part 1): Conceptual model development. *J. Hydrol.* **2017**, *549*, 179–193. [CrossRef]
77. Di, Q.Y.; Fu, C.M.; An, Z.G.; Xu, C.; Wang, Y.L.; Wang, Z.X. Field testing of the surface electromagnetic prospecting system. *Appl. Geophys.* **2017**, *14*, 449–458. [CrossRef]
78. Di, Q.Y.; Wang, M.Y.; Wang, R.; Wang, G.J. Study of the long bipole and large power electromagnetic field. *Chin. J. Geophys.* **2008**, *51*, 1917–1928.
79. Di, Q.Y.; Xue, G.Q.; Lei, D.; Wang, Z.X.; Zhang, Y.M.; Wang, S.; Zhang, Q.M. Geophysical survey over molybdenum mines using the newly developed M-TEM system. *J. Appl. Geophys.* **2018**, *158*, 65–70. [CrossRef]
80. Di, Q.Y.; Wang, M.Y. Determining areas of leakage in the Da Ye Dam using multi-electrode resistivity. *Bull. Eng. Geol. Environ.* **2010**, *69*, 105–109. [CrossRef]
81. Di, Q.Y.; Wang, M.Y. Migration of ground-penetrating radar data method with a finite-element and dispersion. *Geophysics* **2004**, *69*, 472–477. [CrossRef]
82. Di, Q.Y.; Fang, G.Y.; Zhang, Y.M. Research of the Surface Electromagnetic Prospecting (SEP) system. *Chin. J. Geophys.* **2013**, *56*, 3629–3639. [CrossRef]